

# Neural-network-based surrogate model for the properties of neutron stars in 4D Einstein-Gauss-Bonnet gravity

Ioannis Liodis<sup>✉</sup>, Evangelos Smyrniotis<sup>✉</sup>, and Nikolaos Stergioulas

*Department of Physics, Aristotle University of Thessaloniki, 54124 Thessaloniki, Greece*



(Received 9 October 2023; accepted 7 April 2024; published 2 May 2024)

Machine learning and artificial neural networks (ANNs) have increasingly become integral to data analysis research in astrophysics due to the growing demand for fast calculations resulting from the abundance of observational data. Simultaneously, neutron stars and black holes have been extensively examined within modified theories of gravity since they enable the exploration of the strong field regime of gravity. In this study, we employ ANNs to develop a surrogate model for a numerical iterative method to solve the structure equations of neutron stars (NSs) within a specific 4D Einstein-Gauss-Bonnet gravity framework. We have trained highly accurate surrogate models, each corresponding to one of twenty realistic EoSs. The resulting ANN models predict the mass and radius of individual NS models between 10 and 100 times faster than the numerical solver. In the case of batch processing, we demonstrated that the speed up is several orders of magnitude higher. We have trained additional models where the radius is predicted for specific masses. Here, the speed up is considerably higher since the original numerical code that constructs the equilibrium models would have to do additional iterations to find a model with a specific mass. Our ANN models can be used to speed up Bayesian inference, where the mass and radius of equilibrium models in this theory of gravity are required.

DOI: [10.1103/PhysRevD.109.104008](https://doi.org/10.1103/PhysRevD.109.104008)

## I. INTRODUCTION

Recent years have witnessed an abundance of observational data on neutron stars (NSs) coming both from gravitational wave detectors, namely Advanced LIGO [1] and Advanced Virgo [2], and electromagnetic radiation, like the NICER mission [3]. These astrophysical observations have facilitated a significant number of attempts to constrain the EoS of NSs, including the NICER mass and radius measurements [4–6], the tidal deformability measurement through GWs [7–12], as well as joint constraints, e.g., [13–22]. Especially the binary NS merger detection GW170817 [23,24] has sparked further studies in this field [25–32].

Several studies have employed artificial neural networks (ANNs) to reconstruct the EoS of NSs based on their observable properties [33–37]. For instance, [38] investigated the use of ANNs supported by the autoencoder architecture, while [39,40] employed ANNs to represent the EoS in a model-independent way, exploiting the unsupervised automatic differentiation framework. Additional machine-learning techniques have been applied to investigate the NS EoS. For example, in [41], a clustering method was utilized to identify patterns in mass-radius curves, and [42] explored correlations among different EoSs of dense matter using unsupervised machine learning (ML) techniques. Furthermore, attempts have been made to derive nuclear matter characteristics from NS EoS and observations using deep neural networks, see, e.g., [43,44].

NSs have also been the subject of theoretical investigations within alternative theories of gravity—see [45,46]

for comprehensive reviews and possible tests and [47] for the particular theory considered in this work. In particular, the high mass of the secondary component in the GW190814 event [48] has attracted significant interest, as it can only be explained in general relativity (GR) under extreme conditions. Specifically, the only possibilities of this object being a NS is either having an extremely stiff EoS or being the fastest rotating NS ever observed [49–54]. Alternative approaches based on modified gravity theories have been proposed to address this issue as well [55,56]. Namely, [57] explored the issue of the maximum mass of NSs, taking into account the thin-shell effect (chameleon screening) on the NS mass-radius relation while considering a soft EoS, thereby demonstrating the possibility of attaining large masses and explaining the secondary component of GW190814 using modified gravity. Additionally, studies involving modified gravity and the GW170817 event have been conducted [58,59].

Common methods implemented when attempting to infer the NS EoS from observations of their macroscopic properties are based on Bayesian statistics [6,13–20,60]. The majority of these algorithms demand a TOV solver to run numerous times before obtaining the final posterior distribution of various parameters. If we wish to incorporate modified theories of gravity in these studies, we will need a modified TOV solver, like the one presented in [47]. However, this specific algorithm is based on an iterative method for solving the system of differential equations, making Bayesian inference computationally expensive. In any case, solving differential equations numerically thousands or

millions of times is significantly time-consuming and can even prove impractical. Therefore, it would be extremely useful to find an alternative way to quickly yet accurately predict the macroscopic properties of NSs, given some defining characteristics or other macroscopic properties of each equilibrium model. Moreover, the construction of surrogate models for quick evaluation of NS's parameters in modified gravity has already been addressed by recent works [61].

Driven by the aforementioned motivation, this work focuses on implementing ANN regression for two types of functions:  $f_1(\text{EoS}; \alpha, p_c) \rightarrow (M, R)$  and  $f_2(\text{EoS}; \alpha, M) \rightarrow R$ . Here, the EoS represents a distinct variable, since each type includes one ANN model for each EoS.  $\alpha$  is the coupling constant of the theory, and  $p_c$  is the central pressure of the NS. The first type serves as a surrogate model for the numerical iterative method described in [47], which provides the mass and radius of NSs for a specific EoS and a given pair of  $\alpha$  and  $p_c$ . The primary objective is to accelerate the process while maintaining strict accuracy boundaries. The second type cannot be obtained directly using the iterative method since  $p_c$  ought to be an input. Consequently, implementing a root-finding algorithm would be the only solution, resulting in further time delays. Conversely, training ANNs to predict  $R$  based on  $(\text{EoS}; \alpha, M)$  offers a more straightforward approach to handle type  $f_2$ . To the best of our knowledge, this is the first work that employs ANNs to predict the bulk properties of NSs within a modified theory of gravity.

This concept of ANN surrogate models can be implemented in any theory as long as there is a corresponding numerical solver to create a dataset for regression. However, the modified theory of gravity studied in this work is a particular 4D Horndeski scalar-tensor model originating from higher dimensional Einstein-Gauss-Bonnet gravity. The action under consideration is [47]

$$S = \frac{1}{2\kappa} \int d^4x \sqrt{-g} (R + \alpha \mathcal{L}) + S_m, \quad (1)$$

where  $\kappa = \frac{8\pi G}{c^4}$ ,  $S_m$  is the matter Lagrangian and

$$\mathcal{L} = [\phi \mathcal{G} + 4G_{\mu\nu} \nabla^\mu \phi \nabla^\nu \phi - 4(\nabla \phi)^2 \square \phi + 2(\nabla \phi)^4], \quad (2)$$

where  $\mathcal{G}$  is the Gauss-Bonnet scalar

$$\mathcal{G} = R^2 - 4R_{\mu\nu} R^{\mu\nu} + R_{\mu\nu\rho\sigma} R^{\mu\nu\rho\sigma}. \quad (3)$$

The scalar is considered dimensionless, leaving the coupling constant  $\alpha$  with dimensions of length squared.

In our work, we are interested in nonrotating relativistic stars, and thus, we briefly present the differential equations considered in [47] in the Komatsu-Eriguchi-Hachisu (KEH)/Cook-Shapiro-Teukolsky (CST) numerical scheme. The line element describing the spacetime geometry of a

spherically symmetric star in equilibrium using isotropic coordinates is

$$ds^2 = -e^{2\nu} dt^2 + e^{2\mu} [dr^2 + r^2(d\theta^2 + \sin^2 \theta d\varphi^2)], \quad (4)$$

where  $\nu(r)$  and  $\mu(r)$  are metric functions. For the theory under consideration, one can obtain the field equations, which are elliptic equations for the metric functions

$$\nabla^2 \nu = S_\nu(r), \quad (5a)$$

$$\nabla^2 \mu = S_\mu(r), \quad (5b)$$

where  $\nabla^2 = \partial_{rr} + \frac{2}{r} \partial_r$  is the flat-space Laplacian and  $S_\nu, S_\mu$  are the source terms of the elliptic equations. The Green's function of the three-dimensional Laplacian operator in spherical coordinates is then used to obtain integral equations. For the scalar field, the equation can be cast in the form of a current conservation equation, see Eq. (A.4) in [47].

Finally, one has to add the hydrostatic equilibrium equation

$$\nabla_\alpha (H - \ln u^t) = 0, \quad (6)$$

where  $u^t = e^{-\nu}$  and  $H$  is the specific enthalpy

$$H(P) = \int_0^P \frac{dP'}{\epsilon(P') + P'}. \quad (7)$$

By fixing, e.g., the central pressure of the star and starting with a trial value for the central value of the scalar field, an iterative numerical method relaxes to the equilibrium solution, using appropriate boundary conditions at infinity.

## II. DATA

The datasets were generated using the numerical code described in [47]. This code requires the coupling constant  $\alpha[\text{km}^2]$  of the theory and the central pressure  $p_c[10^{35} \text{ dyn/cm}^2]$  of the NS as inputs to compute the corresponding mass  $M[M_\odot]$  and radius  $R[\text{km}]$ . We are using gravitational mass, which also has contributions from the scalar field in the alternative theory we adopt in this paper, hence higher mass values can be attained. In [47] the gravitational mass is extracted from the asymptotic behavior of stationary solutions. For each type of function, we created 20 datasets, one for each of the 20 realistic EoSs listed in Table I and used in [62]. Finally, to enhance the training,  $(M, R, p_c)$  data were logarithmized, and the entire dataset was standardized.<sup>1</sup>

<sup>1</sup>Standardization refers to scaling the data to have zero mean and unit variance to improve the training process of the neural network. For the standardization we used <https://scikit-learn.org/stable/modules/generated/sklearn.preprocessing.StandardScaler.html>.

TABLE I. Numbering of the EoSs used.

Name	Number #
APR	1
BHBLP	2
DD2	3
eosAU	4
eosUU	5
BSk20	6
LS220	7
LS375	8
GS1	9
GS2	10
APR3 (PP)	11
ENG (PP)	12
GNH3 (PP)	13
H4 (PP)	14
MPA1 (PP)	15
SLy4 (PP)	16
WFF2 (PP)	17
SFHo	18
TM1	19
TMA	20

Type  $f_1(\text{EoS}; \alpha, p_c) \rightarrow (M, R)$ . Each dataset for this type consists of 51 values of  $\alpha \in [-10, 70] \times 200$  values of  $p_c \in [0.1, 1.2p_{\max}]$ . The  $\alpha$  values were evenly spaced on a linear scale, while the  $p_c$  values were logarithmically spaced. Here,  $p_{\max}$  represents the central pressure required for a NS to reach its maximum mass for a specific value of the coupling constant. The upper bound of  $p_c$  was chosen to ensure it remains significantly away from the boundary of the stable  $M - R$ , branch to avoid training difficulties in areas of interest. As a representative example, Fig. 1 illustrates for EoS BSk20 that each  $(\alpha, p_c)$  pair corresponds to a unique  $(M, R)$  pair, rendering the training of the ANN relatively straightforward, even when considering a portion of the unstable  $M - R$  branch. The same holds for any other EoS in our chosen set.

Type  $f_2(\text{EoS}; \alpha, M) \rightarrow R$ . The datasets for this type have the same size as those for  $f_1$ , but the range of  $p_c$  values was selected differently. The data now consist of 51 values of  $\alpha \in [-10, 70] \times 200$  values of  $p_c \in [0.1, p_{\max}]$ . This choice is motivated by examining Fig. 1. For a specific EoS, the inputs are  $\alpha$ , which constrains the regression surface to a single curve, and  $M$ , the remaining variable to determine the output  $R$ . In case the  $M - R$  curve for a specific value of  $\alpha$  is non-monotonic, then  $f_2$  is not even a function by definition since it would map a single value of its domain (e.g.,  $M_0$ , where  $|M_0 - M_{\max}| \ll 1$ ) to two different values of its codomain (e.g.,  $R_1, R_2$ ). Therefore, the data must be monotonically increasing or decreasing to ensure the function is well defined.

### III. TRAINING AND TESTING

In this work, the TensorFlow module KERAS<sup>2</sup> was used. For each case, a random selection was made to create a train-test ratio of 70:30. The mean square error (MSE) was chosen as the loss function, while the absolute relative error (ARE) served as the criterion for testing the trained models. A systematic investigation of the network architecture revealed that models with an odd number of dense hidden layers, with a symmetric number of neurons (i.e., 25-35-25) and with alternating two activation functions among the layers (namely “tanh” and “relu”) performed better, with lower final loss and mean ARE (MARE). Based on these findings, the final architecture for each type is shown in Table II. Initial training attempts involved implementing every optimizer from the list of provided KERAS optimizers.<sup>3</sup> However, none of the results were optimal, indicating that the *architecture error*, as defined in [63], was not the dominant source of error. The *optimization error* was further investigated, leading to the implementation of the second-order Broyden–Fletcher–Goldfarb–Shanno optimizer algorithm (BFGS), as suggested in [63]. Incorporating BFGS into the training process was not straightforward, as it is not included in the list of provided KERAS optimizers. Following a similar approach as described in [64] for BFGS (instead of L-BFGS), the final loss decreased by up to four orders of magnitude and reached a stable value. The number of total iterations and the final training loss for each EoS are provided in the Appendix, section A.

### IV. RESULTS

#### A. Training and testing results

Figures 2 and 3 provide indicative training results for  $f_1$  and  $f_2$ , respectively. More specifically, Figs. 2(a) and 3(a) compare the real to the predicted output. Figures 2(b) and 3(b) show the training loss per iteration in terms of the mean square error (MSE) and Figs. 2(c) and 3(c) present the absolute relative error (ARE) on the test set. The MSE was chosen as the loss function from KERAS’ regression loss functions,<sup>4</sup> using the automatic reduction type. The ARE is defined as

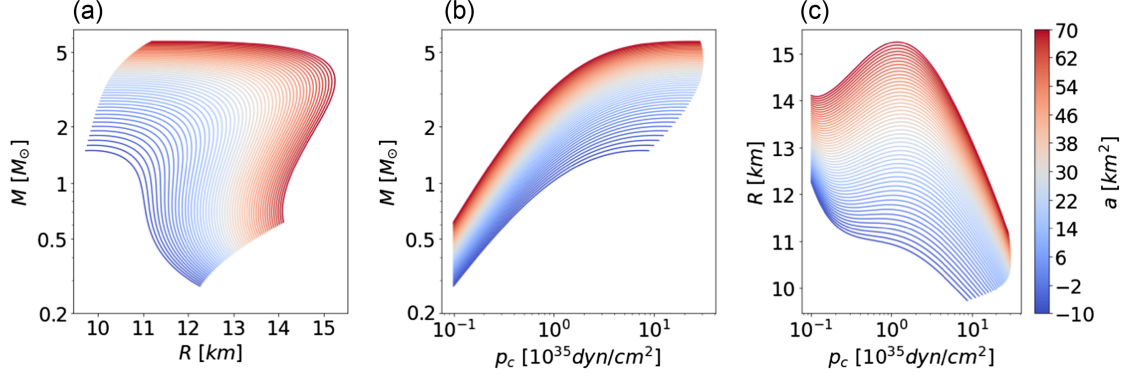
$$\text{ARE}_i = \frac{1}{m} \sum_{j=1}^m \left| \frac{Y_i^j - Y_{i,\text{true}}^j}{Y_{i,\text{true}}^j} \right|, \quad (8)$$

where  $m$  is the number of output neurons,  $Y_i^j$  is the network output with index  $j$  for test point with index  $i$ , and  $Y_{i,\text{true}}^j$  is

<sup>2</sup>[https://www.tensorflow.org/api\\_docs/python/tf/keras](https://www.tensorflow.org/api_docs/python/tf/keras).

<sup>3</sup>[https://www.tensorflow.org/api\\_docs/python/tf/keras/optimizers](https://www.tensorflow.org/api_docs/python/tf/keras/optimizers).

<sup>4</sup>[https://keras.io/api/losses/regression\\_losses/](https://keras.io/api/losses/regression_losses/).


 FIG. 1. Data set for BSk20, regarding type  $f_1$ .

the corresponding real output. The mean ARE (MARE) is defined as:

$$\text{MARE} = \frac{1}{n} \sum_{i=1}^n \text{ARE}_i = \frac{1}{m} \sum_{j=1}^m \left( \frac{1}{n} \sum_{i=1}^n \left| \frac{Y_i^j - Y_{i,\text{true}}^j}{Y_{i,\text{true}}^j} \right| \right), \quad (9)$$

where  $n = 3060$  is the number of points in the test dataset. For  $f_1$  models  $m = 2$ , since there are two output variables ( $M, R$ ), while for  $f_2$  models  $m = 1$  since there is only one output variable ( $R$ ).

Figure 4 depicts the MARE and the maximum ARE on the test set for each EoS, denoted by their corresponding numbers in Table I. Both types ( $f_1$  and  $f_2$ ) exhibit similar mean behavior on the respective test sets for every EoS, with the MARE ranging between  $10^{-5}$  and  $10^{-4}$ . The maximum ARE is  $6 \times 10^{-4}$  for  $f_1$  and  $9 \times 10^{-3}$  for  $f_2$ , demonstrating that in the whole domain of the training and test sets, the absolute relative error never exceeds 1%. In Appendix B, we present a more detailed investigation of the distribution of errors in the domain of the training and test sets. Finally, in Appendix C, we examine the gradients' ( $dR/dM$ ) ARE distribution for both  $f_1$  and  $f_2$ .

### B. $f_1$ speed up

To assess the speed-up achieved when using the trained ANN models of  $f_1$  instead of the numerical code, the dataset corresponding to type  $f_2$  was selected. This dataset consists of 51 values of  $\alpha \in [-10, 70] \times 200$  values of  $p_c \in [0.1, p_{\text{max}}]$ . The choice of this dataset for  $f_1$  is based

on the significance of speed-up in areas of interest, specifically the stable branch of  $M - R$  curves (i.e., for central pressures up to the maximum-mass configuration,  $p_{\text{max}}$ ). The *speed-up*  $s$  is defined as:

$$s = \frac{\Delta t_{\text{ANN}}}{\Delta t_{\text{num}}}, \quad (10)$$

where  $\Delta t_{\text{ANN}}$  is the run time when using an ANN model and  $\Delta t_{\text{num}}$  the run time of the numerical code with the iterative numerical scheme. It is important to note that in our tests, the ANN models ran on an 8-core AMD Ryzen 7 3800X CPU with 16 GB RAM, while the numerical code can only use one such core, no matter how many cores a processor has, and 8 GB RAM. In principle, running the ANN code on a modern GPU could result in an even higher speed up. The reason we compare the performance on a CPU only is to get an estimate of the speed up in existing applications, such as Bayesian inference, where our ANN model can be integrated without necessarily relying on a GPU.

Next, we present three different ways to calculate the output of the models. The speed-up depends on each one of them. It is essential to highlight that by saying *the models*, we refer to the 20 already trained models (one for each EoS), which correspond to  $f_1$ . The three different ways<sup>5</sup> are

- (i) `model.predict(X)`, with  $X$  being one input value,
- (ii) `model(X)`, with  $X$  being one input value,
- (iii) `model.predict(X)`, with  $\mathbf{X}$  being an array of input values.

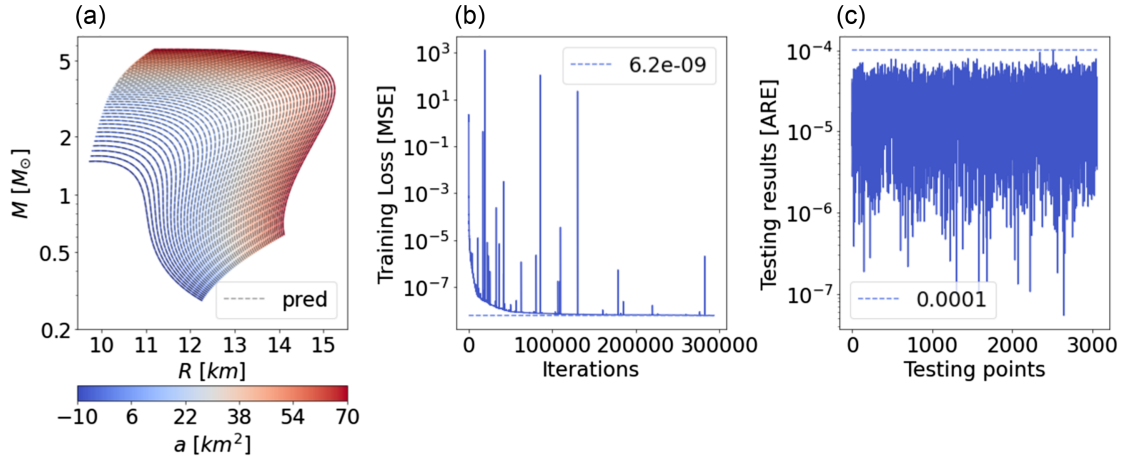
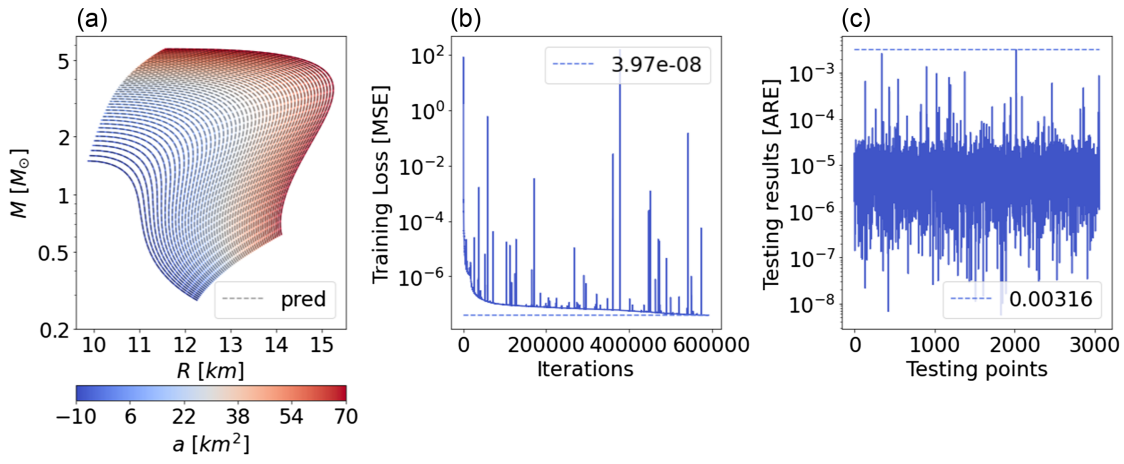
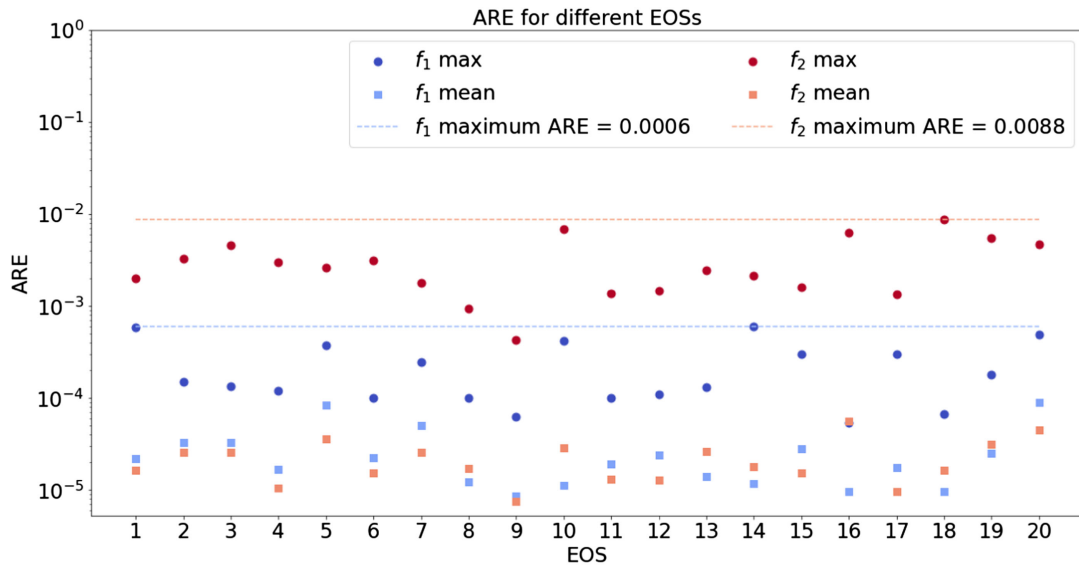
Since Bayesian inference algorithms mainly require one ( $M, R$ ) pair per iteration, ways (i) and (iii) are presented separately, although they use the same function (*predict*) to calculate the outputs. In the next paragraphs, we will

<sup>5</sup>The difference lies in the way these functions are designed. `model.predict(X)` calls can scale to very large arrays, while `model(X)` happens in-memory and does not scale. For further details the reader is referred to [https://keras.io/getting\\_started/faq/](https://keras.io/getting_started/faq/).

TABLE II. Final network architecture.

Layer	Type $f_1$	Type $f_2$
Input layer	$(\alpha, p_c)$	$(\alpha, M)$
Hidden layer 1	25-tanh	25-tanh
Hidden layer 2	35-relu	35-relu
Hidden layer 3	25-tanh	25-tanh
Output layer	$(M, R)$	$R$



FIG. 2. Training results for  $f_1$  and BSk20.FIG. 3. Training results for  $f_2$  and BSk20.FIG. 4.  $f_1$  and  $f_2$  absolute relative errors on the testing set.

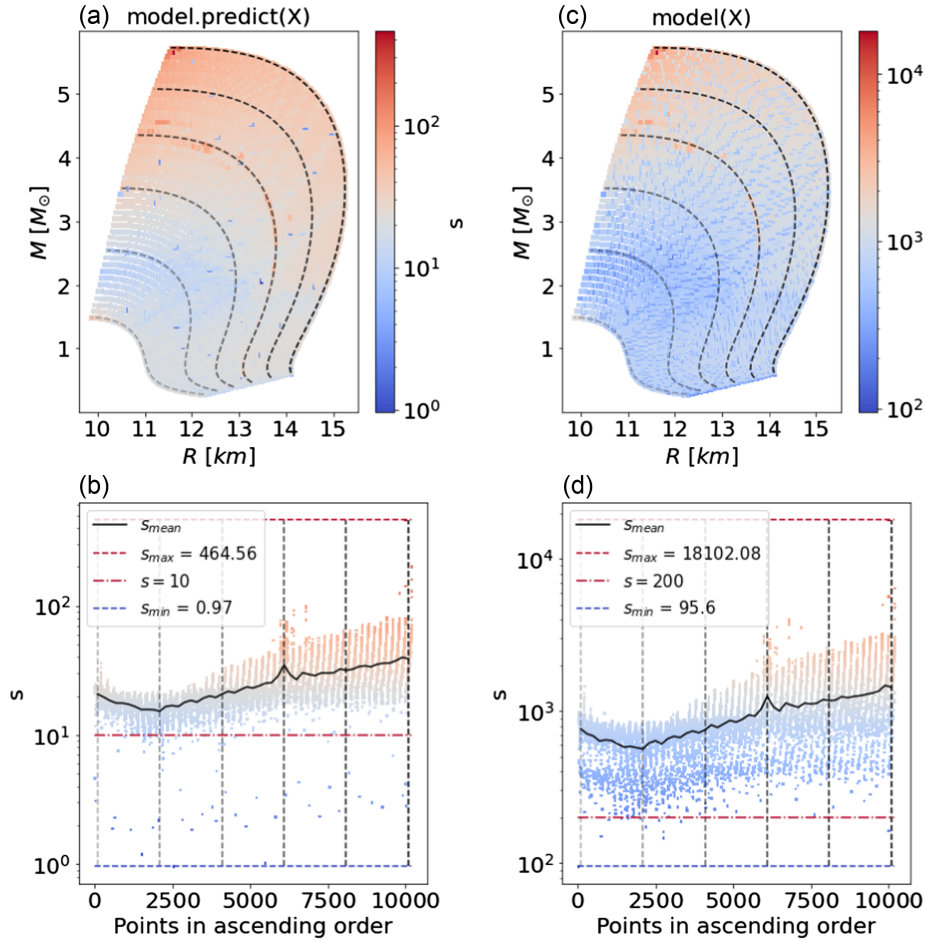


FIG. 5. Speed up per  $M - R$  data point showing how many times faster the trained ANN model is than the numerical code in each case.

present the different speed-ups each of these ways achieves, as well as some other differences they demonstrate.

### 1. *model.predict* (X)

The left panel of Fig. 5 illustrates the speed up for the first case. In panel 5(a), the color represents the speed up, and the dashed lines with increasing transparency correspond to six different  $M - R$  curves, for  $a = \{-10, 6, 22, 38, 54, 70\}$  km<sup>2</sup>, respectively. Panel 5(b) illustrates the speed-up values for a specific arrangement of the data points. These are arranged in increasing order of  $\alpha$ , and for each  $\alpha$ , they are also arranged in increasing order with respect to  $p_c$ . The color still represents the speed-up values, and each black vertical dashed line corresponds to the same transparency level as in panel 5(a), aiding visualization and establishing the connection between the two plots. Each point on the solid black line represents the mean value of the speed up  $s$  for the 200 points comprising the corresponding  $M - R$  curve of a specific value of  $\alpha$ . The general trend reveals a minimum on the second vertical dashed line, followed by an increase in performance. It is also evident that the majority of speed-up values range between 10 and 100 (less than 1% is outside of this range). As a general trend,

higher speed-ups are observed for larger input values. The mean speed up, considering all data points, is  $\sim 25$ .

### 2. *model* (X)

The right panel of Fig. 5 illustrates the speed up for the *model* (X) case, and its configuration is similar to the left panel. It is evident that there is an increase of *two orders of magnitude* in speed up. The majority of speed-up values range between 200 and 18000 (less than 0.2% is outside of this range). The mean speed up, considering all data points, is  $> 900$ .

### 3. *model.predict* (X)

In this case, the  $N = 51 \times 200 = 10200$  data points were inserted as an array of input values  $\mathbf{X}$ . Thus, there is no direct way of comparing its speed to the previous cases. Yet, to give some intuition on the acceleration that this way (of calling the model) provides, we can calculate the *effective run time*  $\Delta t_{\text{eff}}$ , which we define as

$$\Delta t_{\text{eff}} = \frac{\Delta t_N}{N}, \quad (11)$$

TABLE III. Speed up comparison.

Numerical code run time	(Mean) 1003.5 ms	(Min) 147.96 ms	(Max) 18122.4 ms
Output method	Speed up (Mean)	Speed up (Min)	Speed up (Max)
model.predict ( $X$ )	25.12	0.97	464.56
model ( $X$ )	921.9	95.6	18102.1
model.predict ( $\mathbf{X}$ )	31295.5	4614.5	565157.2

where  $\Delta t_N$  is the *total run time* for the whole array as input. For  $N = 10200$  the resulting speed-ups are presented in Table III, together with all the previous speed-ups. The first line of the table provides information about the run time of the numerical code that uses the iterative numerical scheme. The other lines show the corresponding speed-ups. Going from the first to the second and then to the third method, the speed-up increases by 1.5 to 2 orders of magnitude each time.

Comparing `model.predict ( $X$ )` to `model.predict ( $\mathbf{X}$ )` it is obvious that the latter does not have a linear behavior regarding the size of  $\mathbf{X}$ . This is attributed to the way this function manipulates vectorized data, which is designed for batch processing of large numbers of inputs. Therefore, when it is possible to vectorize the data into large batches the `model.predict ()` function should be preferred. On the contrary, when one needs to iterate over the data and small numbers of inputs are manipulated, `model ()` should be preferred.

## V. SUMMARY AND DISCUSSION

The aim of this work was to explore the application of ANNs in predicting the mass-radius relation of NSs for chosen EoSs in a specific alternative theory of gravity. The datasets used in this study were generated using an iterative numerical code. For each EoS, each equilibrium model is defined by the value of the coupling constant  $\alpha$  of the specific theory of gravity and the central pressure  $p_c$  of the NS. Two types of functions,  $f_1$  and  $f_2$ , were considered, each with its own input and output parameters.

For  $f_1$ , the datasets included 51 values of  $\alpha$  ranging from -10 to 70 and 200 values of  $p_c$  ranging from  $10^{24}$  dyn/cm<sup>2</sup> to 1.2 times the maximum central pressure ( $p_{\max}$ ) for each specific EoS. The objective was to predict the NS's mass and radius based on the given values of  $\alpha$  and  $p_c$ . On the other hand,  $f_2$  focused on predicting the NS's radius given the  $\alpha$  and a fixed value of  $M$  for each EoS.

The training and test phase used a train-to-test ratio of 70:30, with the mean square error selected as the loss function and the absolute relative error chosen as the testing criterion. An investigation of different ANN architectures revealed that models with an odd number of hidden layers, a symmetric distribution of neurons, and alternating activation functions “tanh” and “relu” exhibited lower final

loss and mean absolute relative error. The final architecture chosen for training was “dense 25 tanh—dense 35 relu—dense 25 tanh”.

The results demonstrate that the trained ANN models provide accurate predictions for both  $f_1$  and  $f_2$ . The test phase showed that the MARE ranged between  $10^{-5}$  and  $10^{-4}$ , indicating the models' ability to capture the mass-radius relation of NSs across different EoSs. The maximum ARE was  $6 \times 10^{-4}$  for  $f_1$  and  $9 \times 10^{-3}$  for  $f_2$ , never exceeding 1% in the whole domain of the training and test sets.

Furthermore, the  $f_1$  speed-up was analyzed to assess the performance improvement achieved using the trained ANN model instead of the iterative numerical code. The results revealed significant acceleration, with most speed-up values (when computing individual models) ranging from 10 to 100, depending on the input parameters. When the ANN processed a whole array of values, the speed up was several orders of magnitude higher. For  $f_2$  the speed up is even higher since the iterative numerical code needs to perform additional iteration to find a model with specific mass.

All the constructed models can make accurate predictions in a very short time compared to the iterative numerical solver of differential equations. Therefore, the ANN models can replace the iterative numerical code in Bayesian inference algorithms, paving the way for fast and viable investigations, e.g., of the degeneracy between the uncertainties of the EoS and the theory of gravity.

It is important to note that further investigations can be pursued to enhance the accuracy and efficiency of the trained ANN models. Future research could explore alternative architectures, optimization algorithms, and additional input parameters to refine the predictions. However, for most practical applications, the accuracy achieved here will be more than sufficient.

Another potential extension is to include additional macroscopic NS parameters, which will not significantly increase execution time, although it may increase the complexity of training. Namely, the tidal deformability could be added as an extra parameter to be mapped by the network models whose run time, after being trained, depends only on the models' architecture. Computing the tidal deformability adds just one more equation to the

TOV system of equations, so it only somewhat increases the total computational time. Provided that training data are available for this specific theory, our ANN models can be extended to also predict this parameter.

In conclusion, this study successfully employed ANNs to predict the mass-radius relation of NSs for different EoS in a specific alternative theory of gravity. The trained models exhibited high accuracy. Furthermore, this research offers a valuable tool for Bayesian inference methods. The speed-up achieved through the trained ANN models allows for a more efficient exploration of the parameter space. We plan to construct similar ANN models also for other theories of gravity and for parameterized EoS formulations.

The resulting ANN models of this work are available at the repository [65].

### ACKNOWLEDGMENTS

We are grateful to Alexandra Eleni Koloniari, Bhaskar Biswas, and Paraskevi Nousi for their comments.

### APPENDIX A: TRAINING ITERATIONS AND FINAL LOSS

Figure 6 demonstrates the final loss and the number of iterations for each training. The number of iterations ranges between  $10^4$  and  $10^6$  while the MSE of the final loss ranges between  $8 \times 10^{-10}$  and  $10^{-6}$ . The inconsistency of iterations among training for different EoSs is attributed to the algorithm used for optimization since the number of BFGS iterations is not the same as the number of iterations presented in Fig. 6. The common variable of every training is the “maximum iterations”, which is the BFGS iterations,

and it was set to 230000, not the total iterations. The latter is the quantity of loss-function assessments and will be higher than the maximum iterations since each BFGS iteration must calculate the loss function and the gradients numerous times. There was the case that the algorithm stopped earlier, which indicates that additional stopping conditions were in effect (i.e., the losses did not significantly vary between two iterations).

One can notice that for every EoS,  $f_1$  models reached a lower final loss than  $f_2$  models, although based on the dimensionality, the training should be easier for  $f_2$ . The discrepancy is attributed to the training data difficulty in specific regions for  $f_2$  (i.e., for high  $M$  values and every  $\alpha$  the curves are almost horizontal), which leads to Appendix B.

### APPENDIX B: LARGE ARES IN $f_2$

As mentioned in Sec. IV A when discussing Fig. 4, the maximum ARES on the testing set for  $f_2$  are systematically higher compared to  $f_1$ , although the MAREs do not demonstrate the same behavior. This is attributed to the nature of  $f_2$  data, since for one  $\alpha$  and as  $M$  increases, the  $M - R$  curve reaches an almost horizontal region, making the gradient of  $f_2$  very large. This is implied in Fig. 3, which, compared to Fig. 2, demonstrates larger upper spikes in the testing results. To support this statement, Fig. 7 is presented, where  $M_n$  merely corresponds to the number of  $M$  points for every  $a = \text{const.}$  curve, in increasing order.  $M_n$  is used instead of  $M$  just to compare the data from every EoS. The top plot of Fig. 7 shows the ARES for every input pair and a specific EoS. Here, the ARES are calculated on the whole dataset. One can notice that the larger ARES are located at the right edge, corresponding to large  $M_n$  values, while the remaining

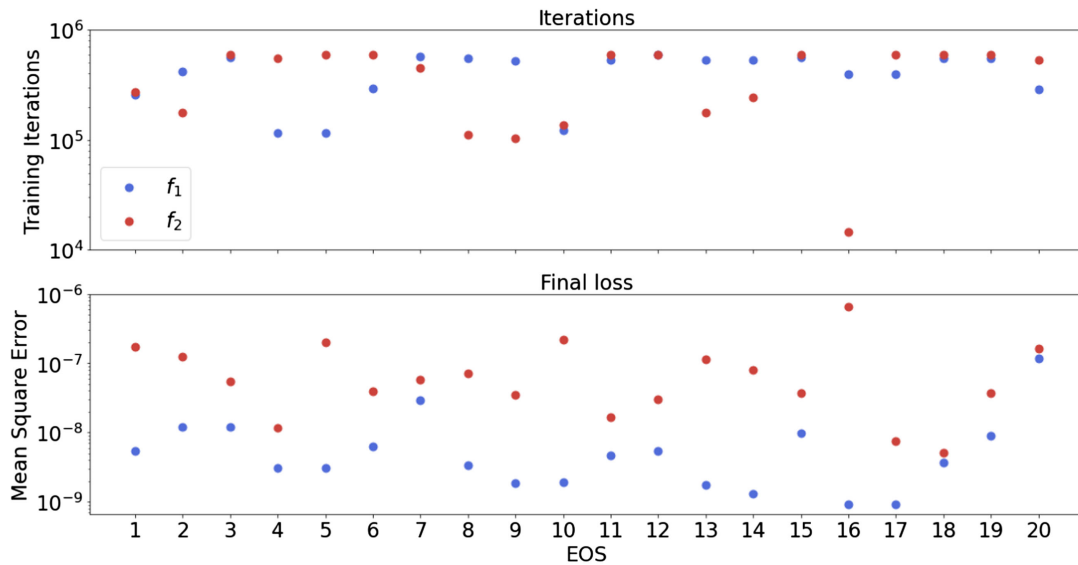


FIG. 6. Iterations and final loss for  $f_1$  and  $f_2$ .



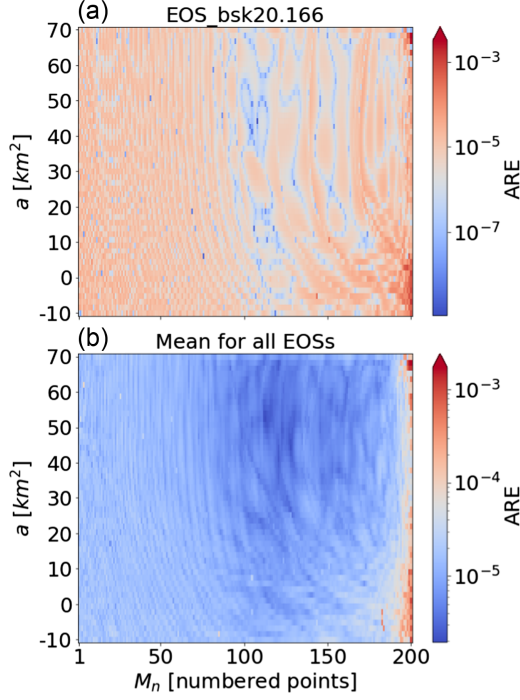


FIG. 7. (a)  $f_2$  AREs for BSk20 and (b) mean AREs for every EoS.  $M_n$  is the numbered  $M$  points with ascending order, ranging from 1–200.

area seems uniform, except for some local structures of very small AREs. The bottom plot of Fig. 7 shows the mean AREs for all EoSs and for every input pair—which would not be possible if it was not for  $M_n$ . Note that these values are not MAREs since MARE refers to mean with respect to data points of the same EoS. Indeed, the mean values demonstrate a uniform behavior around  $10^{-5}$ , while the right edge is over two orders of magnitude higher. It is, therefore, evident that the largest AREs are located in the near-horizontal region of  $M - R$  curves (i.e., for  $M_n$  near 200).

### APPENDIX C: GRADIENTS' ARES

It is often necessary to know the accuracy of the gradients  $dR/dM$ , for instance when performing gradient-based Bayesian inference methods. An estimate of this error can be calculated by taking the AREs between these numerical derivatives on the simulated data and the models' predictions. Note that the AREs manipulated in this context are given by

$$\text{ARE}_i = \left| \frac{Y_{i,\text{pred}} - Y_{i,\text{true}}}{Y_{i,\text{true}}} \right|, \quad (\text{C1})$$

where

$$Y_{i,\text{true}} = \frac{R_{i+1}^{\text{true}} - R_i^{\text{true}}}{M_{i+1}^{\text{true}} - M_i^{\text{true}}}, \quad (\text{C2})$$

and

$$Y_{i,\text{pred}} = \begin{cases} \frac{R_{i+1}^{\text{pred}} - R_i^{\text{pred}}}{M_{i+1}^{\text{pred}} - M_i^{\text{pred}}}, & \text{for } f_1 \\ \frac{R_{i+1}^{\text{pred}} - R_i^{\text{pred}}}{M_{i+1}^{\text{true}} - M_i^{\text{true}}}, & \text{for } f_2. \end{cases} \quad (\text{C3})$$

We use forward numerical differentiation and compare the predicted derivatives to their true values. Notice that  $f_2$  does not predict the mass and therefore  $M_i^{\text{true}}$  must be used for these values.

Some limitations of this approach should also be noted before proceeding with the findings. First, the simulated data points are 200 for each EoS and coupling constant value. Hence, the resolution is not sufficiently high for the forward differences to approach the infinitesimal limit. Furthermore, even if we assume numerical differences to sufficiently approximate the true derivatives, they will not always be finite and non-zero by construction. That is, in the high-mass regime,  $dR/dM$  increases significantly, becoming infinite on the maximum mass for each  $M - R$  curve. Therefore, it is difficult to calculate a reliable error in this region. This is also the case where  $dR/dM$  is zero. Therefore, we *a priori* expect high AREs where the  $M - R$  curves are locally horizontal or vertical.

Figure 8 shows the calculated AREs. Panels (a) and (b) refer to the  $f_1$  and  $f_2$  data, respectively, and to the BSk20 EoS. The color represents the logarithm of the ARE at each point, whose scale is given in the color bar placed as the y-axis of panel (c). The latter panel shows the distributions of the AREs for  $f_1$  (green) and  $f_2$  (red), with the x-axis representing the counts of ARE values inside a bin. We can distinguish a peak around zero ( $\text{ARE} = 10^0$ ), which is attributed to one specific EoS, APR. Excluding the AREs of APR EoS from the histogram, we end up with  $f_1$  selected, which indeed does not contain the peak. In this panel, a Gaussian distribution is also plotted with a dotted line. Its mean and standard deviation is given by the mean and sample standard deviation of the ARE values of  $f_2$  ( $\mu = -2.373$ ,  $\sigma = 0.901$ ). It is evident that both the  $f_1$  selected and  $f_2$  AREs are drawn from practically the same normal distribution.

Regarding the spatial features of AREs, it is important to remember that the  $f_1$  data are slightly extended to the unstable  $M - R$  branches, as described in Sec. II. In panel (a) one can see that there are two regions with high errors:  $dR/dM \rightarrow \infty$  and  $dR/dM \rightarrow 0$ . The first region is found in the high-mass regime, where  $M - R$  curves are locally horizontal, while the second is found in the low-mass regime, where  $M - R$  curves are locally vertical. The regions where  $dR/dM$  is infinite or zero are colored dark red, since the AREs are very high, as expected. This is also the case for  $f_2$ , with the only difference being in the

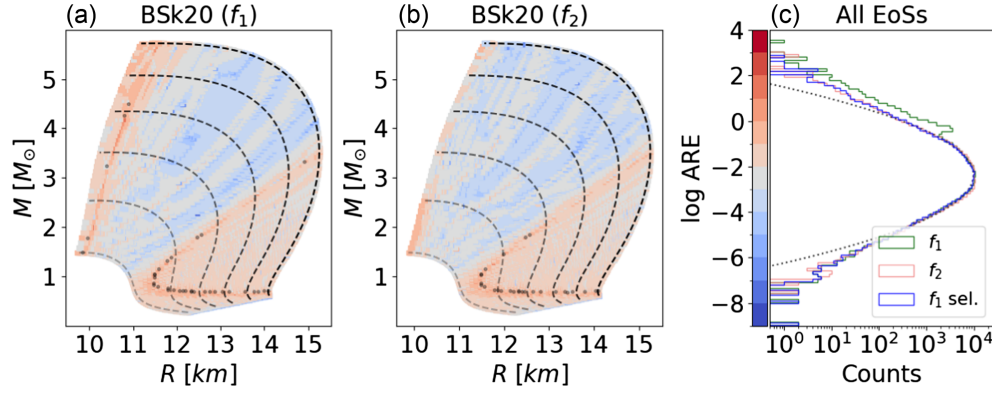


FIG. 8. (a)  $f_1$  gradients' AREs and (b)  $f_2$  gradients AREs, for BSk20. The gray dots mark the points where the monotonicity is not preserved. (c) AREs distributions for all EoSs, for  $f_1$ ,  $f_2$ , and  $f_1$  selected, which merely excludes one specific EoS (APR).

high-mass regime, due to the selection of data (as described in Sec. II). Notice that, at points where  $dR/dM$  is infinite or zero monotonicity is not preserved [gray dots in panels (a) and (b)], which means that the true and predicted gradients do not have the same sign.

For intermediate masses, the gradients take finite and nonzero values, so the AREs are generally lower than  $10^{-2}$ . This is the region which is the most reliable to examine the AREs. It is thus safe to trust the models' monotonicity where the true gradients are not zero or infinity.

- 
- [1] J. Aasi *et al.*, Advanced LIGO, *Classical Quantum Gravity* **32**, 074001 (2015).
  - [2] F. Acernese *et al.*, Advanced Virgo: A second-generation interferometric gravitational wave detector, *Classical Quantum Gravity* **32**, 024001 (2014).
  - [3] Z. Arzoumanian *et al.*, The neutron star interior composition explorer (NICER): Mission definition, in *Space Telescopes and Instrumentation 2014: Ultraviolet to Gamma Ray*, Society of Photo-Optical Instrumentation Engineers (SPIE) Conference Series Vol. 9144, edited by T. Takahashi, J.-W. A. den Herder, and M. Bautz (2014), p. 914420, 10.1117/12.2056811.
  - [4] T. E. Riley, A. L. Watts, S. Bogdanov, P. S. Ray, R. M. Ludlam, S. Guillot, Z. Arzoumanian, C. L. Baker, A. V. Bilous, D. Chakrabarty, K. C. Gendreau, A. K. Harding, W. C. G. Ho, J. M. Lattimer, S. M. Morsink, and T. E. Strohmayer, A nicer view of PSR J0030 + 0451: Millisecond pulsar parameter estimation, *Astrophys. J.* **887**, L21 (2019).
  - [5] M. C. Miller *et al.*, PSR J0030 + 0451 mass and radius from NICER data and implications for the properties of neutron star matter, *Astrophys. J. Lett.* **887**, L24 (2019).
  - [6] M. C. Miller *et al.*, The radius of PSR J0740 + 6620 from NICER and XMM-Newton data, *Astrophys. J. Lett.* **918**, L28 (2021).
  - [7] E. D. V. Oeveren and J. L. Friedman, Upper limit set by causality on the tidal deformability of a neutron star, *Phys. Rev. D* **95**, 083014 (2017).
  - [8] T. Hinderer, Tidal Love numbers of neutron stars, *Astrophys. J.* **677**, 1216 (2008).
  - [9] T. Binnington and E. Poisson, Relativistic theory of tidal Love numbers, *Phys. Rev. D* **80**, 084018 (2009).
  - [10] T. Damour and A. Nagar, Relativistic tidal properties of neutron stars, *Phys. Rev. D* **80**, 084035 (2009).
  - [11] K. Chatziioannou, Neutron-star tidal deformability and equation-of-state constraints, *Gen. Relativ. Gravit.* **52**, 109 (2020).
  - [12] T. Dietrich, T. Hinderer, and A. Samajdar, Interpreting binary neutron star mergers: Describing the binary neutron star dynamics, modelling gravitational waveforms, and analyzing detections, *Gen. Relativ. Gravit.* **53**, 27 (2021).
  - [13] G. Raaijmakers, S. K. Greif, T. E. Riley, T. Hinderer, K. Hebeler, A. Schwenk, A. L. Watts, S. Nissanke, S. Guillot, J. M. Lattimer, and R. M. Ludlam, Constraining the dense matter equation of state with joint analysis of NICER and LIGO/virgo measurements, *Astrophys. J.* **893**, L21 (2020).
  - [14] B. Biswas and S. Datta, Constraining neutron star properties with a new equation of state insensitive approach, *Phys. Rev. D* **106**, 043012 (2022).
  - [15] B. Biswas, Impact of PREX-II and combined radio/NICER/XMM-Newton's mass-radius measurement of PSR J0740 + 6620 on the dense-matter equation of state, *Astrophys. J.* **921**, 63 (2021).
  - [16] B. Biswas, Bayesian model selection of neutron star equations of state using multi-messenger observations, *Astrophys. J.* **926**, 75 (2022).

- [17] S. Traversi, P. Char, and G. Pagliara, Bayesian inference of dense matter equation of state within relativistic mean field models using astrophysical measurements, *Astrophys. J.* **897**, 165 (2020).
- [18] W.-J. Xie and B.-A. Li, Bayesian inference of high-density nuclear symmetry energy from radii of canonical neutron stars, *Astrophys. J.* **883**, 174 (2019).
- [19] B. Biswas, P. Char, R. Nandi, and S. Bose, Towards mitigation of apparent tension between nuclear physics and astrophysical observations by improved modeling of neutron star matter, *Phys. Rev. D* **103**, 103015 (2021).
- [20] T. Dietrich, M. W. Coughlin, P. T. H. Pang, M. Bulla, J. Heinzel, L. Issa, I. Tews, and S. Antier, Multimessenger constraints on the neutron-star equation of state and the Hubble constant, *Science* **370**, 1450 (2020).
- [21] P. Landry, R. Essick, and K. Chatziioannou, Nonparametric constraints on neutron star matter with existing and upcoming gravitational wave and pulsar observations, *Phys. Rev. D* **101**, 123007 (2020).
- [22] G. Raaijmakers, S. K. Greif, K. Hebeler, T. Hinderer, S. Nisanke, A. Schwenk, T. E. Riley, A. L. Watts, J. M. Lattimer, and W. C. G. Ho, Constraints on the dense matter equation of state and neutron star properties from NICER's mass-radius estimate of PSR J0740 + 6620 and multimessenger observations, *Astrophys. J. Lett.* **918**, L29 (2021).
- [23] B. P. Abbott *et al.* (LIGO Scientific and Virgo Collaborations), GW170817: Observation of gravitational waves from a binary neutron star inspiral, *Phys. Rev. Lett.* **119**, 161101 (2017).
- [24] B. P. Abbott *et al.* (LIGO Scientific and Virgo Collaborations), Properties of the binary neutron star merger GW170817, *Phys. Rev. X* **9**, 011001 (2019).
- [25] J.-L. Jiang, S.-P. Tang, D.-S. Shao, M.-Z. Han, Y.-J. Li, Y.-Z. Wang, Z.-P. Jin, Y.-Z. Fan, and D.-M. Wei, The equation of state and some key parameters of neutron stars: Constraints from GW170817, the nuclear data, and the low-mass x-ray binary data, *Astrophys. J.* **885**, 39 (2019).
- [26] F. J. Fattoyev, J. Piekarewicz, and C. J. Horowitz, Neutron skins and neutron stars in the multimessenger era, *Phys. Rev. Lett.* **120**, 172702 (2018).
- [27] E. R. Most, L. R. Weih, L. Rezzolla, and J. Schaffner-Bielich, New constraints on radii and tidal deformabilities of neutron stars from GW170817, *Phys. Rev. Lett.* **120**, 261103 (2018).
- [28] B. P. Abbott *et al.* (LIGO Scientific and Virgo Collaborations), GW170817: Measurements of neutron star radii and equation of state, *Phys. Rev. Lett.* **121**, 161101 (2018).
- [29] P. Landry and B. Kumar, Constraints on the moment of inertia of PSR J0737-3039A from GW170817, *Astrophys. J. Lett.* **868**, L22 (2018).
- [30] E. Annala, T. Gorda, A. Kurkela, and A. Vuorinen, Gravitational-wave constraints on the neutron-star-matter equation of state, *Phys. Rev. Lett.* **120**, 172703 (2018).
- [31] Y. Lim and J. W. Holt, Neutron star tidal deformabilities constrained by nuclear theory and experiment, *Phys. Rev. Lett.* **121**, 062701 (2018).
- [32] B. Kumar and P. Landry, Inferring neutron star properties from GW170817 with universal relations, *Phys. Rev. D* **99**, 123026 (2019).
- [33] Y. Fujimoto, K. Fukushima, and K. Murase, Mapping neutron star data to the equation of state using the deep neural network, *Phys. Rev. D* **101**, 054016 (2020).
- [34] Y. Fujimoto, K. Fukushima, and K. Murase, Methodology study of machine learning for the neutron star equation of state, *Phys. Rev. D* **98**, 023019 (2018).
- [35] Y. Fujimoto, K. Fukushima, and K. Murase, Extensive studies of the neutron star equation of state from the deep learning inference with the observational data augmentation, *J. High Energy Phys.* **03** (2021) 273.
- [36] M. Ferreira and C. Providência, Unveiling the nuclear matter EoS from neutron star properties: A supervised machine learning approach, *J. Cosmol. Astropart. Phys.* **07** (2021) 011.
- [37] P. G. Krastev, Translating neutron star observations to nuclear symmetry energy via deep neural networks, *Galaxies* **10**, 16 (2022).
- [38] F. Morawski and M. Bejger, Neural network reconstruction of the dense matter equation of state derived from the parameters of neutron stars, *Astron. Astrophys.* **642**, 8 (2020).
- [39] S. Soma, L. Wang, S. Shi, H. Stöcker, and K. Zhou, Neural network reconstruction of the dense matter equation of state from neutron star observables, *J. Cosmol. Astropart. Phys.* **08** (2022) 071.
- [40] S. Soma, L. Wang, S. Shi, H. Stöcker, and K. Zhou, Reconstructing the neutron star equation of state from observational data via automatic differentiation, *Phys. Rev. D* **107**, 083028 (2023).
- [41] R. V. Lobato, E. V. Chmianski, and C. A. Bertulani, Cluster structures with machine learning support in neutron star M-R relations, *J. Phys. Conf. Ser.* **2340**, 012014 (2022).
- [42] R. V. Lobato, E. V. Chmianski, and C. A. Bertulani, Unsupervised machine learning correlations in eos of neutron stars, *Proc. Sci. XVHadronPhysics* (2022) 062.
- [43] M. Ferreira, V. Carvalho, and C. Providência, Extracting nuclear matter properties from the neutron star matter equation of state using deep neural networks, *Phys. Rev. D* **106**, 103023 (2022).
- [44] P. G. Krastev, A deep learning approach to extracting nuclear matter properties from neutron star observations, *Symmetry* **15**, 1123 (2023).
- [45] D. D. Doneva, F. M. Ramazanoğlu, H. O. Silva, T. P. Sotiriou, and S. S. Yazadjiev, Spontaneous scalarization, *Rev. Mod. Phys.* **96**, 015004 (2024).
- [46] E. Berti *et al.*, Testing general relativity with present and future astrophysical observations, *Classical Quantum Gravity* **32**, 243001 (2015).
- [47] C. Charmousis, A. Lehé bel, E. Smyrniotis, and N. Stergioulas, Astrophysical constraints on compact objects in 4D Einstein-Gauss-Bonnet gravity, *J. Cosmol. Astropart. Phys.* **02** (2022) 033.
- [48] R. Abbott *et al.* (LIGO Scientific and Virgo Collaborations), GW190814: Gravitational waves from the coalescence of a 23 solar mass black hole with a 2.6 solar mass compact object, *Astrophys. J. Lett.* **896**, L44 (2020).

- [49] K. Huang, J. Hu, Y. Zhang, and H. Shen, The possibility of the secondary object in GW190814 as a neutron star, *Astrophys. J.* **904**, 39 (2020).
- [50] I. Bombaci, A. Drago, D. Logoteta, G. Pagliara, and I. Vidaña, Was GW190814 a black hole–strange quark star system?, *Phys. Rev. Lett.* **126**, 162702 (2021).
- [51] Z. Roupas, G. Panotopoulos, and I. Lopes, QCD color superconductivity in compact stars: Color-flavor locked quark star candidate for the gravitational-wave signal GW190814, *Phys. Rev. D* **103**, 083015 (2021).
- [52] X. Zhou, A. Li, and B.-A. Li, R-mode stability of GW190814's secondary component as a supermassive and superfast pulsar, *Astrophys. J.* **910**, 62 (2021).
- [53] N.-B. Zhang and B.-A. Li, GW190814's secondary component with mass  $2.50\text{--}2.67M_{\odot}$  as a superfast pulsar, *Astrophys. J.* **902**, 38 (2020).
- [54] B. Biswas, R. Nandi, P. Char, S. Bose, and N. Stergioulas, GW190814: On the properties of the secondary component of the binary, *Mon. Not. R. Astron. Soc.* **505**, 1600 (2021).
- [55] A. Astashenok, S. Capozziello, S. Odintsov, and V. Oikonomou, Extended gravity description for the GW190814 supermassive neutron star, *Phys. Lett. B* **811**, 135910 (2020).
- [56] A. Astashenok, S. Capozziello, S. Odintsov, and V. Oikonomou, Causal limit of neutron star maximum mass in  $f(R)$  gravity in view of GW190814, *Phys. Lett. B* **816**, 136222 (2021).
- [57] R. C. Nunes, J. G. Coelho, and J. C. N. de Araujo, Weighing massive neutron star with screening gravity: A look on PSR J0740 + 6620 and GW190814 secondary component, *Eur. Phys. J. C* **80**, 1115 (2020).
- [58] R. Lobato, O. Lourenço, P. Moraes, C. Lenzi, M. de Avellar, W. de Paula, M. Dutra, and M. Malheiro, Neutron stars in  $f(\mathcal{R}, T)$  gravity using realistic equations of state in the light of massive pulsars and GW170817, *J. Cosmol. Astropart. Phys.* **12** (2020) 039.
- [59] R. V. Lobato, G. A. Carvalho, and C. A. Bertulani, Neutron stars in  $f(R, L_m)$  gravity with realistic equations of state: Joint-constraints with GW170817, massive pulsars, and the PSR J0030 + 0451 mass-radius from NICER data, *Eur. Phys. J. C* **81**, 1013 (2021).
- [60] M. Al-Mamun, A. W. Steiner, J. Nättilä, J. Lange, R. O'Shaughnessy, I. Tews, S. Gandolfi, C. Heinke, and S. Han, Combining electromagnetic and gravitational-wave constraints on neutron-star masses and radii, *Phys. Rev. Lett.* **126**, 061101 (2021).
- [61] M. Guo, J. Zhao, and L. Shao, Extended reduced-order surrogate models for scalar-tensor gravity in the strong field and applications to binary pulsars and gravitational waves, *Phys. Rev. D* **104**, 104065 (2021).
- [62] A. Bauswein, S. Blacker, G. Lioutas, T. Soutanis, V. Vijayan, and N. Stergioulas, Systematics of prompt black-hole formation in neutron star mergers, *Phys. Rev. D* **103**, 123004 (2021).
- [63] E. J. Michaud, Z. Liu, and M. Tegmark, Precision machine learning, *Entropy* **25**, 175 (2023).
- [64] P.-Y. Chuang, Optimize TensorFlow & KERAS models with L-BFGS from TensorFlow Probability (2019), <https://gist.github.com/piyueh/712ec7d4540489aad2dcfb80f9a54993>.
- [65] I. Liodis, ANN surrogate model NS EGB (2023), [10.5281/zenodo.11059404](https://zenodo.org/record/11059404).